Chapter 2

Experimental Apparatus

The E760 experimental area is located in the low dispersion region of the AP-50 section of the Fermilab Antiproton Accumulator. A schematic representation of the Fermilab accelerator complex is shown in figure 2.1. Figure 2.2 shows a schematic representation of the $\bar{p}$ source and where the E760 detector is located in one of the three straight sections.

A cut-through view of the E760 detector is shown in figure 2.3. Attached to the E760 detector, and shown in figure 2.3, is the proton source, gas jet. In this chapter, the antiproton and proton sources are discussed followed by descriptions of the different components of the E760 detector.

2.1 Antiproton Source

The $\bar{p}$ source is described in detail in the Tevatron's design report [59]; a basic outline describing the $\bar{p}$ source is given in this section along with how the $\bar{p}$ beam characteristics are determined. Protons extracted from Fermilab's Main Ring at F0

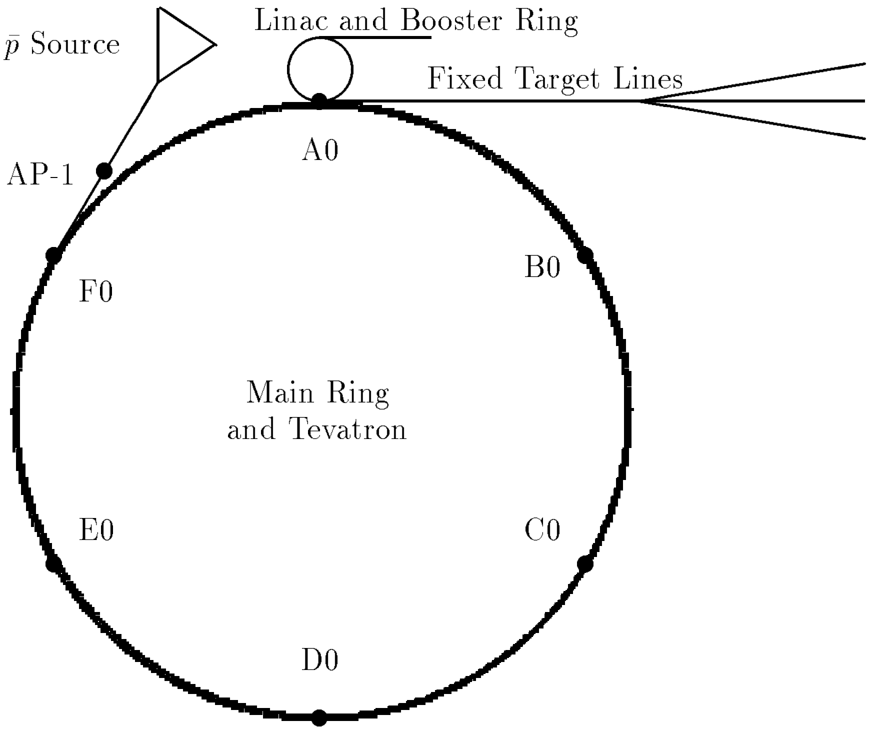

Figure 2.1: A schematic representation of the Fermilab accelerator complex.

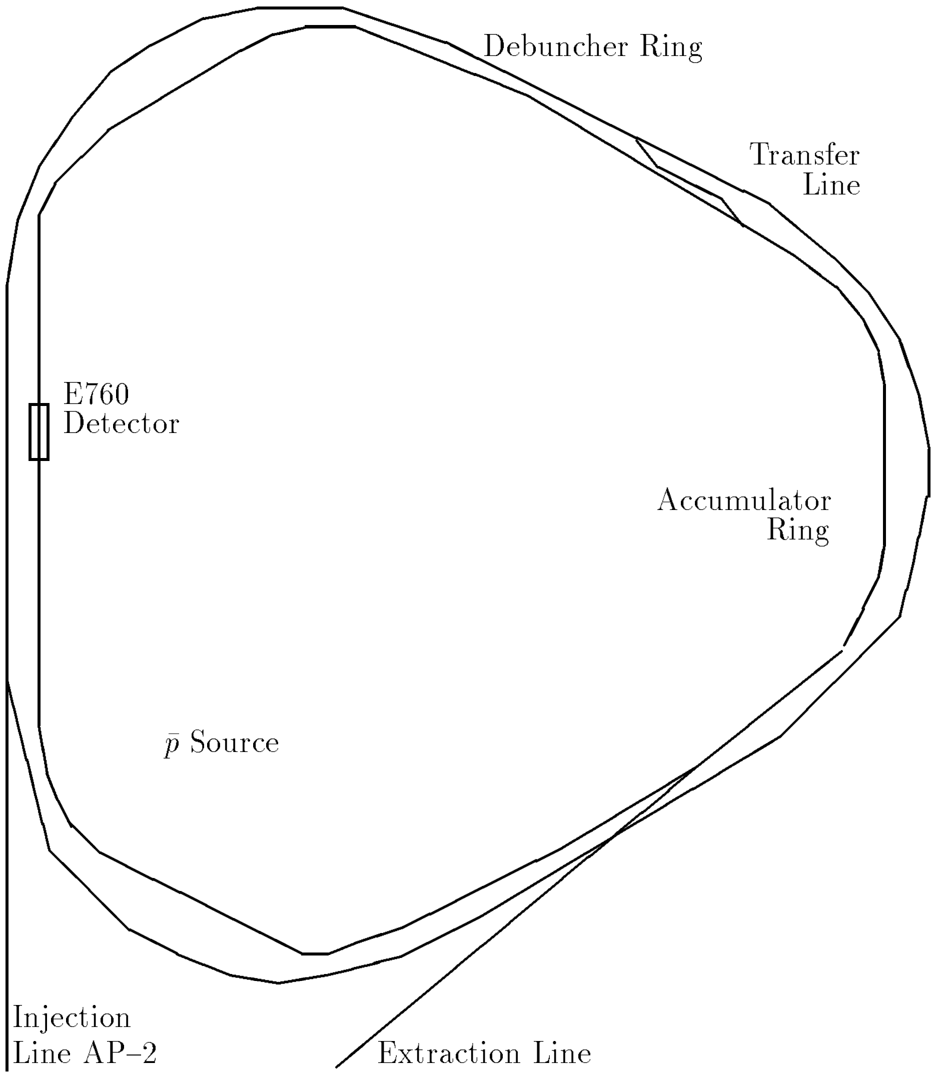

Figure 2.2: A schematic representation of the Fermilab $\bar{p}$ source and the location of E760.

Figure 2.3: A cut-through view of the E760 detector and gas jet.

(see figures 2.1 and 2.2) are transported to the AP-1 target hall. The target, tungsten or tungsten alloy, is 6 cm thick. Each bunch of protons that is sent to the target contains $\approx 10^{12}$ particles. The negatively charged particles produced by the collision of the 120 GeV proton beam and target are collected with a 15 cm long lithium lens with a radius of 1 cm. The lens is pulsed (0.6 msec) with $\approx$ 500 KA to provide a uniform field gradient ($\approx$ 1000 T/m). The greatest number of antiprotons are produced with energies between 8 and 13 GeV. A bending magnet focuses the negatively charged particles with momentum 8.9 GeV/c into the beam transport line. The rest of the particles are contained by a beam dump.

The $\bar{p}$ bunch is injected into the debuncher ring through the connecting AP-2 beam line. The Debuncher accepts the $\bar{p}$ bunch and then stochastically cools the $\bar{p}$'s which spreads the the $\bar{p}$'s out into a beam, i.e. debunches the antiprotons. The spread of momentum $(\frac{\Delta p}{p})_{rms}$ of the $\bar{p}$ beam changes in the debuncher ring from 4% to 0.2%. The $\bar{p}$'s are then transferred to the Accumulator. All pions and muons decay before transfer. Electrons lose energy due to synchrotron radiation and are lost.

The Accumulator accepts $\bar{p}$'s and further cools the beam to a nominal momentum spread of $\approx 0.05\%$. The immediate cooling of each transferred set of $\bar{p}$'s removes the $\bar{p}$'s from the phase space needed to accept the next transfer from the Debuncher. The Debuncher and Accumulator cooling operations occur much more quickly than the interval between main ring bunches of 120 GeV protons on the target. The average number of antiprotons that are collected for every 10^6 protons sent to the target is 3.

Accumulation of antiprotons continues until the number of particles in the beam is $\approx 4 \times 10^{11}$. The beam is then decelerated from 8.9 GeV/c to the appropriate momentum. The desired momentum $p_{\bar{p}}$ as a function of center of mass energy E_{cm} is

$$p_{\bar{p}} = \sqrt{\frac{E_{cm}^4}{4m_p^2} - E_{cm}^2}, \tag{2.1}$$

where m_p is the mass of the proton; the relationship between $p_{\bar{p}}$ and E_{cm} is shown in figure 2.4. Once the desired momentum is reached, the beam is further cooled to $(\frac{\Delta p}{p})_{rms} \approx 2 \times 10^{-4}$.

The momentum is calculated from the revolution frequency of the particles f and the orbit length L,

$$c\beta = fL = f(L_0 + \Delta L), \tag{2.2}$$

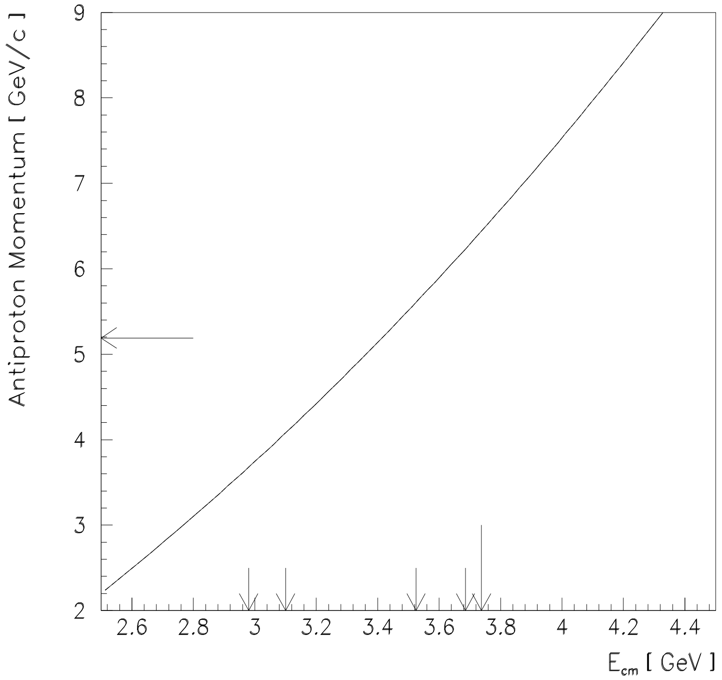

Figure 2.4: The $\bar{p}$ momentum as a function of the energy in the center of momentum frame. The shorter downward arrows point at masses (starting with the smallest energy) η_c, J/ψ, χ_{cog} and ψ', respectively; the larger downward arrow indicates the open charm threshold and the horizontal arrow is the $\bar{p}$ source transition point.

where L_0 is a reference orbit length and ΔL is the difference of the orbit from L_0. The reference orbit [60] is determined from data taken at the ψ'. The orbit length difference ΔL is measured using Beam Position Monitors [61] (BPM); there are 48 BPMs located around the Accumulator Ring.

Keeping the momentum spread of the $\bar{p}$ beam small is important. Stochastic cooling [62] is a technique of using measurements of the beam particles' deviations from the central orbit (longitudinal and transverse) to determine the appropriate kick provided by a kicker magnet, to bring the particles back to the proper orbit. The stochastic cooling keeps the momentum spread small as well as the transverse size of the beam to be less than 0.5 cm (95% containment) in the low dispersion region. The cooling is also used to restore $\bar{p}$'s to the proper orbit and energy after interacting with the gas jet target.

The momentum spread is calculated by

$$\frac{dp}{p} = \frac{1}{\eta}\frac{df}{f}, \tag{2.3}$$

where η, the momentum slip factor, is defined as

$$\eta \equiv \frac{1}{\gamma^2} - \frac{1}{\gamma_t^2} \tag{2.4}$$

and γ_t^2 depends upon the machine lattice and is associated with the transition point. The spread in frequency is determined from the beam current Schottky noise spectrum [63]. Schottky noise bands appear at integer multiples of the beam revolution frequency (dependent upon beam energy, $f_{rev} \approx 0.62$ MHz); a coaxial quarter wavelength resonant pickup with a principal frequency of 79.323 MHz detects the harmonic of the revolution frequency closest to the principal frequency of the pickup (depending upon the beam energy, the 126^{th} to 129^{th} harmonic). The spectral power density $P(f)$ of the noise is proportional to the particle density $\frac{dN}{df}$:

$$P(f)\Delta f = 2\pi(ef)^2\,\frac{dN}{df}\Delta f, \tag{2.5}$$

where e is the charge of the antiproton. A spectrum analyzer[1] is used to analyze the signal; a typical spectrum is shown in figure 2.5. The number of $\bar{p}$'s at a certain frequency, and therefore a specific momentum, is known.

[1]A Hewlett Packard model 8568B analyzer.

Figure 2.5: A typical Schottky power spectrum used to determine beam energy distribution.

The uncertainties of the of the beam energy measurements are discussed in section 7.6. The convolution of the beam energy spread and a Breit-Wigner resonance is presented in section 8.1.

2.2 Proton Source

A molecular hydrogen gas jet provides a proton target nearly at rest. The protons are injected into the Accumulator Ring at 90° to the antiproton beam. The

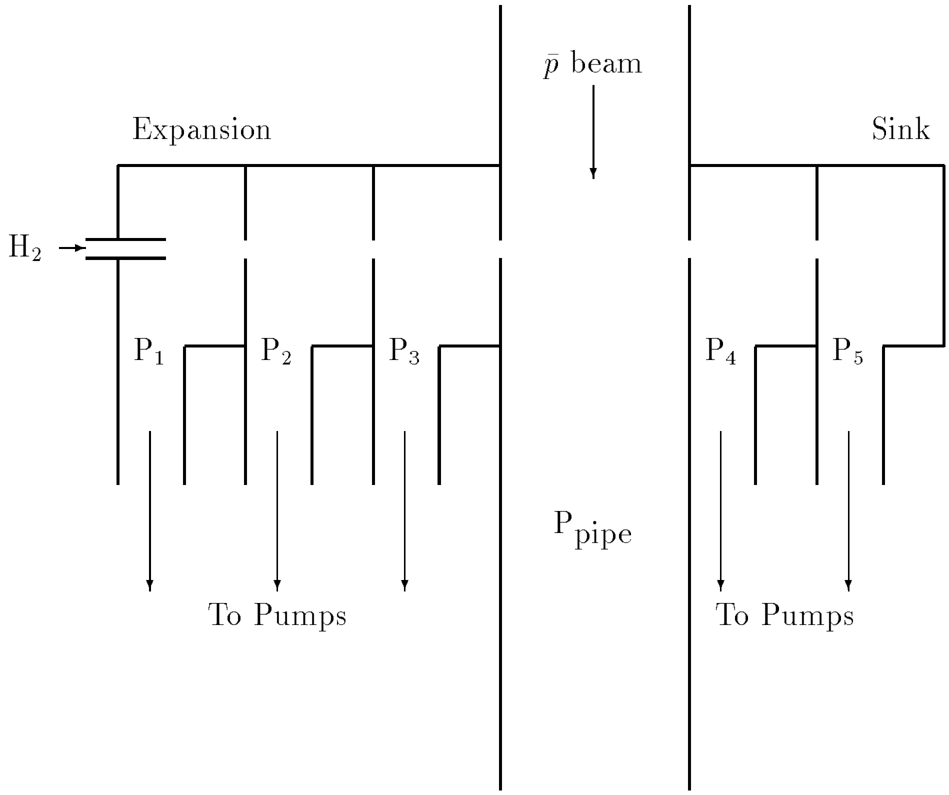

Figure 2.6: A schematic of the molecular hydrogen gas jet. The relationship of the pressures from each chamber and the beam pipe is $P_1 > P_2 > P_3 > P_{pipe} < P_4 < P_5$. The skimmers (not shown) are located around the expansion chambers' exit holes.

accumulator ring is under a vacuum (10^{-8} torr) so as not to scatter $\bar{p}$'s out of the beam pipe. The injection of the hydrogen requires a series of vacuum pumps to be used. A desired point-like interaction region requires that the hydrogen be injected into a small volume and collected quickly with pumps so as not to contaminate the accumulator vacuum. The gas jet apparatus [64],shown schematically in figure 2.6, leads to a dense target of protons and, therefore, a large instantaneous luminosity can be obtained.

The nozzle area of the gas jet and hydrogen are cooled by liquid nitrogen. The low temperature induces hydrogen molecules to cluster. The gas jet has to pass through several chambers. Expansion of the gas in each chamber causes some molecules to be removed from the jet stream by skimmers located around each chamber's exit hole. Vacuum pumps connected to each chamber remove the reflected hydrogen before the gas can exit the chambers and contaminate the accumulator ring vacuum. The resulting gas jet density at the interaction region is typically 3.5×10^{13} atoms/cm^3. The pressure of the hydrogen gas jet, and therefore the gas jet density in the interaction region, can be changed to increase and decrease the instantaneous luminosity.

The transverse dimension of the gas jet[2] when intersecting the $\bar{p}$ beam is < 1 cm^2. With a large beam fill and an orbit frequency ≈ 0.62 MHz, the peak instantaneous luminosity achieved is $\approx 1 \times 10^{31}$ cm^{-2}s^{-1}.

[2]The diameter of the gas jet is 6.3 mm for 95% containment.

Figure 2.7: A typical pulse height spectrum from the luminosity monitor.

2.3 Luminosity Monitor

The luminosity monitor consists of a set of solid state detectors located below the beam pipe. The luminosity monitor's detectors observe and count elastic $\bar{p}p$ scattering near 90° with respect to the $\bar{p}$ beam direction in the lab frame. Several of the detectors are movable to measure the $\bar{p}p$ elastic cross section [65] in the angular region near 90°. A single fixed detector at 86.435° is used to monitor the rate of interactions.

The luminosity is determined from knowledge of the $\bar{p}p$ differential elastic cross section [66] and the acceptance of the fixed detector. The fixed detector is 500 μm thick and covers a 12 mm $\times$ 48 mm area located 1.47 m below the interaction region. The detector is sufficiently thick to stop protons with recoil energy less than 8 MeV. Each pulse height spectrum, a typical example shown in figure 2.7, is fit to the expected spectrum shape and an exponential background. The resulting number of counts over a known time period is used to determine the luminosity. The uncertainties of the luminosity measurement are discussed in section 7.6.

2.4 Hodoscopes

The E760 detector includes three scintillator hodoscopes. Each of the hodoscopes' elements has its signal split between the hardware trigger logic (section 5.2) and pattern units (latch signals above a certain minimum signal height). Two hodoscopes' signals are also split and connected to FERA ADCs for offline pulse height analysis.

The H1 hodoscope consists of 8 sections, each covering an azimuthal octant. The scintillator is $\approx$ 2 mm thick and slightly curved, resulting in the same scintillator thickness traversed by all particles from the interaction region. The H1 hodoscope is the closest detector element to the interaction point (see figure 2.3) and covers polar angles 9° to 65°. The main purpose of the H1 hodoscope is for the hardware trigger. The H1 hodoscope signals are recorded to perform a pulse height analysis.

H2 hodoscope is located at a radial distance of 16.5 cm. The H2 hodoscope covers the polar angles 12° to 65° with 32 elements distributed about the full azimuth

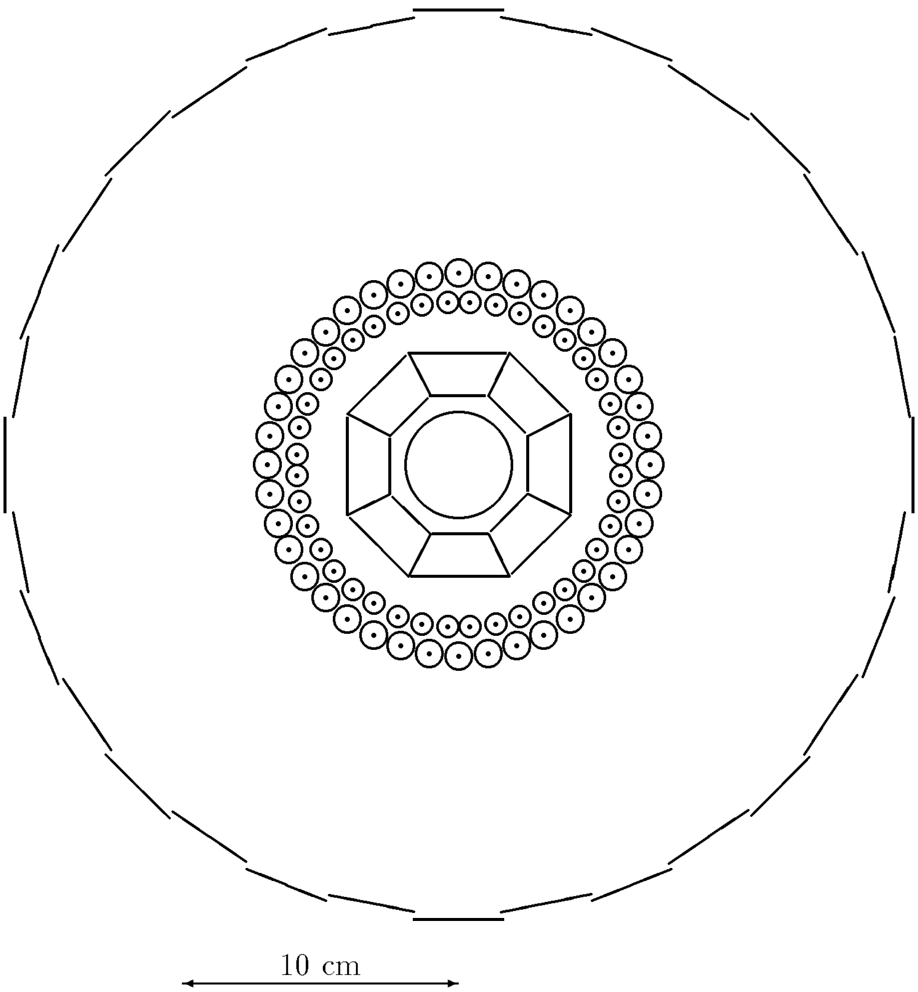

Figure 2.8: A cross sectional ϕ view of the beam pipe surrounded by hodoscopes H1 and H2 separated by the straw tubes. H1 is curved and appears thick when looking along the beam pipe. Not shown between the straw tubes and the H2 hodoscope is the inner tracking detector consisting of the RPC and MWPC.

(see figure 2.8). The thickness of the scintillator is 4 mm. The recorded signals of the H2 hodoscope are used to perform a pulse height analysis to determine the number of charged particles that pass through an H2 element. The H1 and H2 hodoscopes are used to define charged tracks in the hardware trigger logic.

The FCV hodoscope is an eight element full azimuthal detector covering the angles between $2°$ and $9°$. The scintillator is oriented perpendicular to the beam pipe and located ≈ 1.8 m downstream of the interaction target (see figure 2.3). The FCV purpose is to detect forward going charged particles. The FCV and H1 hodoscopes combine to provide a veto of charged particles for the hardware trigger logic for neutral events while covering the entire polar angle subtended by both calorimeters.

2.5 Čerenkov Detector

A threshold Čerenkov detector [67] is used to identify e's (electrons and positrons) while rejecting π's (charged pions). The Čerenkov detector is split into azimuthal octants and covers the polar angles between $15°$ and $70°$. Due to the range of π energies, the large polar angular acceptance, and the range of E_{cm} that E760 investigates, each octant of the Čerenkov detector is split into two polar sections by a 0.3 mm thick aluminum foil septum at $38°$. Different gases are used in the two polar sections and therefore there are different threshold velocities for Čerenkov light production in the sections. A schematic of an octant of the Čerenkov detector is shown in figure 2.9.

Figure 2.9: One octant of the threshold Čerenkov detector. Each polar section uses a different gas; the sections are separated by an aluminum foil septum.

The backward region ($70° < \theta < 38°$) octants use spherically shaped mirrors to reflect the Čerenkov photons onto a second mirror that is observed by a photomultiplier tube. The backward region is filled with Freon13 gas which has threshold momenta for e's and π's of 13.5 MeV/c and 3.68 GeV/c, respectively, since the index of refraction has $(n-1) = 720 \times 10^{-6}$. The forward region ($38° < \theta < 15°$) is filled with CO_2 gas, $(n-1) = 420 \times 10^{-6}$, which results in thresholds of 17.6 MeV/c and 4.82 GeV/c for e's and π's, respectively. A forward octant mirrors is ellipsoidal with the two foci being the interaction region and an observing photomultiplier tube.

Although e^+e^- from any $\bar{c}c$ state have momenta much greater than the Čerenkov threshold, the number of photoelectrons observed ranges from 1 to 20 depending upon the polar angle. At the forward edge of the Čerenkov detector acceptance (15°), a charged pion from $\bar{p}p \to \pi^+\pi^-$ will be above the Čerenkov threshold when E_{cm} is greater than 3.41 GeV. However the number of Čerenkov photons produced by a charged pion is much smaller than from e's and less likely to produce a signal in the photomultiplier tube; therefore discrimination of e's and π's can be accomplished.

2.6 Charged Tracking

The closest charged tracking detector to the interaction point is a two layer set of straw tubes [68] shown in figure 2.8. Each layer consists of forty straw tubes 22 cm long parallel to the beam pipe providing azimuthal angle information. The tubes' centers are located 6 and 7 mm radially from the center of the beam pipe. The inner layer of tubes has a diameter of 8.4 mm and the outer layer a diameter of 9.7 mm. Argon-CO_2-Methane gas is flowed through the straw tubes. Polar angle information is determined from charge division with the distance along the beam pipe measured to $\sigma_z = 1.6$ mm. The drift time is 150 μs and the azimuthal resolution is a few mrad.

Next radially outward is the inner tracking chamber module (see figure 2.3) which consists of two detectors [69] shown schematically in figure 2.10. Closest to the interaction point of the two detectors is a radial projection chamber (RPC); the other detctor is a multi-wire proportional chamber (MWPC). The module is separated into two chambers and employs two gasses: Argon-Ethane and Argon-Isobutane for the RPC and MWPC, respectively. The RPC consists of 80 wires parallel to the beam. Each track is sampled up to sixteen times. Charge division is used for each sampling of the track to help determine the polar angle ($\Delta z = 8$ mm). The MWPC is a set of 320 wires, parallel to the beam. This chamber includes pads etched on the external

Figure 2.10: The inner tracking chamber consisting of a radial projection chamber (RPC) and a multi-wire proportional chamber (MWPC).

cathode to provide polar angle information ($\Delta z = 0.4$ mm). A cross sectional view of the module is in figure 2.11.

The outer most cylindrical tracking detector from the beam pipe is a set of limited streamer tubes (LST) also called Iarocci tubes [70] (labelled as the outer tracking chamber in figure 2.3). The LST consists of two layers of tubes with conductive strips. The conductive strips are oriented longitudinal and transverse providing both azimuthal and polar information. Argon-Isobutane-CO_2 gas is flowed in this chamber. The LST covers polar angles between 22° and 60°.

A forward tracking chamber (FTC) is a flat disc multi-wire proportional chamber with its wires oriented perpendicular to the beam pipe. Located at the downstream end of the Čerenkov detector (see figure 2.3), the FTC covers the polar angles

Figure 2.11: A cross sectional view of the RPC and MWPC. The shaded region is a drift cell in the RPC.

between $10°$ and $18°$. The FTC consists of 3 sets of wires oriented at $60°$ to one another. Argon-Isobutane is used in the FTC.

The last tracking detector is located 2.7 m downstream of the interaction point and is oriented perpendicular to the beam pipe (the forward straw tubes in figure 2.3). Four sets of straw tubes cover the forward end cap calorimeter. The four sets are at orientations that are $45°$ to one another. The forward straw tubes are filled with Argon-Ethane gas.

2.7 Forward End Cap Calorimeter

The electromagnetic forward end cap calorimeter [71] consists of 144 rectangular modules arranged in a 13×13 array (see figure 2.12). At each corner of the array there are no modules since these would be behind the central calorimeter. There is

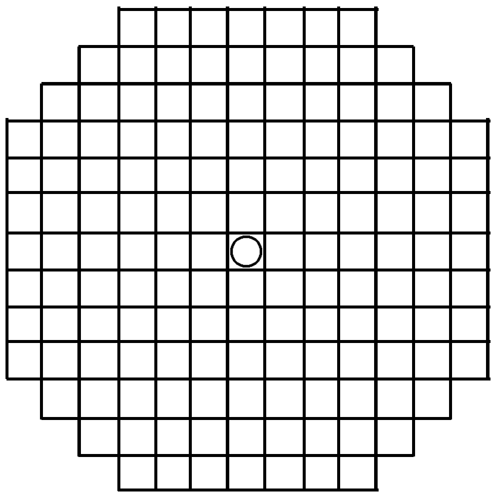

Figure 2.12: A schematic of the forward end cap calorimeter 13×13 array with no corner modules. There is no middle module to allow the beam pipe to pass.

Figure 2.13: A schematic of forward calorimeter module; the layers of the module are described in the text.

no central module for the passage of the beam pipe. The polar angles between 2° and 10° are covered by the forward end cap calorimeter.

Each module consists of 148 layers of alternating lead and scintillator; a schematic of a module is shown in figure 2.13. The transverse dimensions of these layers are 10×10 cm^2. The lead plates are 1 mm thick and the scintillator slabs are 0.64 cm and 0.32 cm thick. The thinner scintillator plates are used alternately with the thicker ones for the back half of each module. Overall the modules are 14.7 radiation lengths. A waveshifter plate $10.0 \times 0.64 \times 51.7$ cm^3 is attached to a side of each module. The waveshifter plate extends past the end of the module and is optically coupled to a photomultiplier tube for detecting light from the scintillators.

2.8 Central Calorimeter

The electromagnetic central calorimeter [72] is the focal point of the E760 detector. Each counter is a lead-glass block and an attached photomultiplier tube. The counters are arranged in a cylindrical 20×64 array ($\theta \times \phi$) totaling 1280 counters and every counter points back to the interaction region. The 64 counters at the same θ in the array are considered a *ring*. The lead-glass blocks are different sizes for the different rings. The central calorimeter covers the angles from 70° to 10° with the rings (and shapes) numbered 1 to 20, respectively (see figure 3.1). The 20 counters from different rings at the same ϕ in the array make up the contents of a *wedge*. The construction of the counters and calorimeter is discussed in the next chapter.

Wedge Numbers from a Ring	Super-wedge Number
1– 9	1
9–17	2
17–25	3
25–33	4
33–41	5
41–49	6
49–57	7
57– 1	8

Table 2.1: The summing pattern for the Level I Summers defining super-wedges for any given ring.

2.9 Central Calorimeter Summers

Although not literally a component of the detector, the central calorimeter summers [73] are used not only for triggering but as a way to determine whether a signal in the central calorimeter is from the interaction of interest (the triggered event) or from another interaction before or after the triggered upon interaction, also known as *pile-up* (discussed in section 6.4). A description of the summed central calorimeter signals follows; figure 2.14 shows how the central calorimeter summer modules are implemented.

The Level I Summer modules split each counter's signal; the majority of the signal (97%) is sent onto the FERA ADCs for recording the signal of each central calorimeter counter. The leftover part of the signal is used in a sum. Each Level I Summer module corresponds to a ring of counters. The counters' signals are summed into octant known as *super-wedges*. Counters at the edge of the octants are used in two Level I sums (see table 2.1). The total number of Level I summed signals for the

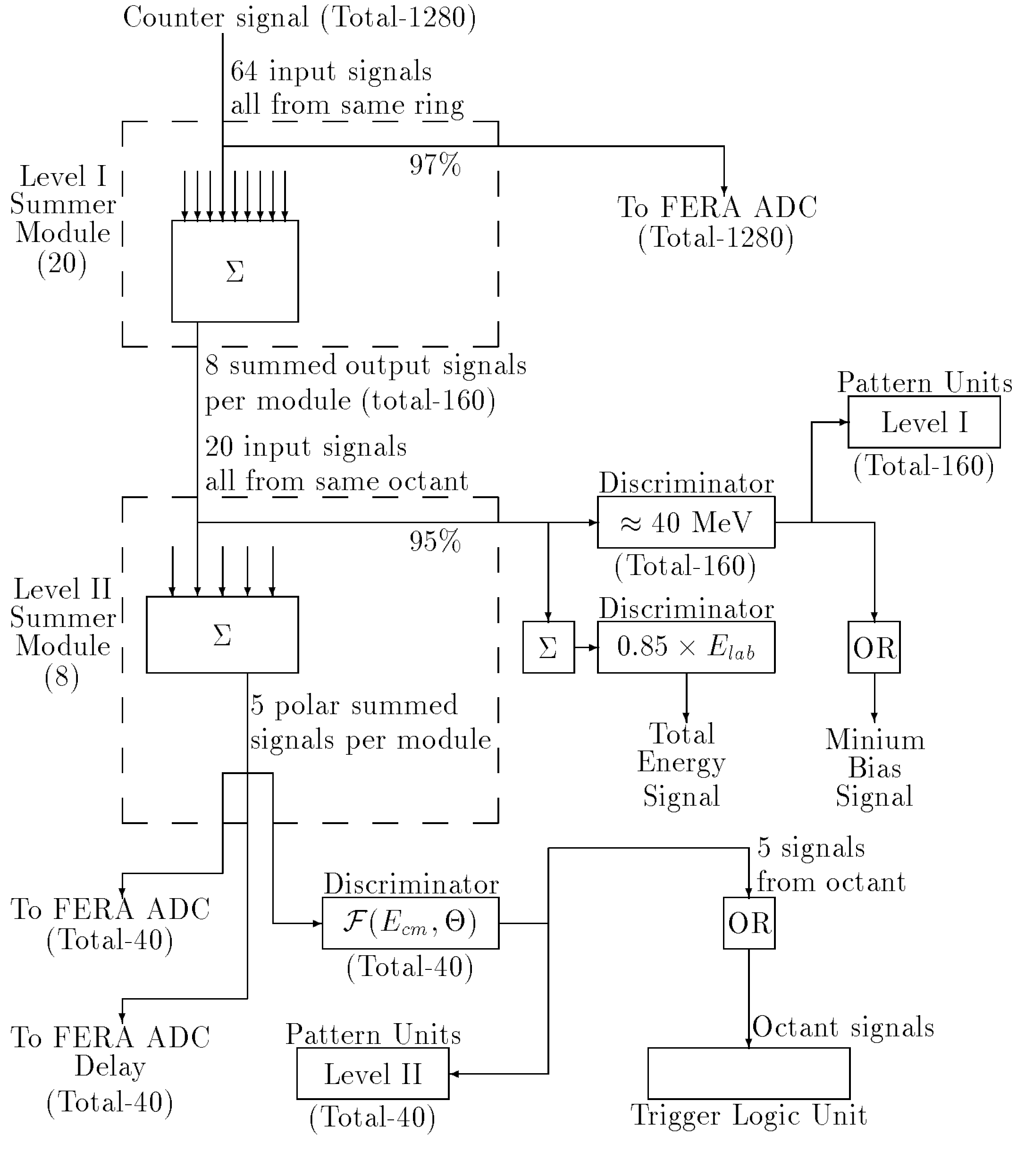

Figure 2.14: A schematic of the hardware logic that includes the central calorimeter summer modules. 1280 central calorimeter counter signals are summed into 160 Level I summed signals (which are also used to from a minimum bias signal), 40 Level II summed signals, and 1 total energy signal.

Ring Numbers from a Super-wedge	Super-ring Number
1– 4	1
4– 8	2
8–12	3
12–16	4
16–20	5

Table 2.2: The summing pattern for the Level II Summers defining super-rings.

twenty modules is ($\theta \times \Phi$) $20 \times 8 = 160$. The module amplifies the summed signals; these signals are the input signals to the Level II Summer modules.

The Level II Summer modules split the input signals and pass 95% to 160 discriminators which have a common threshold of approximately 40 MeV. This forms the minimum bias and timing of the trigger (see section 5.2). The discriminators are also connected to latches: the Level I pattern units. The 160 Level I signals are also summed to form a total energy trigger which is used in the hardware trigger.

The remaining parts of the split signals in the Level II summer modules, a module for each octant, are weighted, summed and amplified in five polar intervals (*super-rings*) resulting in ($\Theta \times \Phi$) $5 \times 8 = 40$ Level II signals, also known as *super-blocks*. The super-wedge signals from certain rings which are at the boundary between super-blocks, are used in two Level II sums (see table 2.2). Figure 2.15 shows a beam's view of the calorimeter and marks the areas that are super-blocks.

The weighted summed Level II signals form three sets of signals, 40 Level II super-block signals per set. One set of signals from each super-ring is sent to discriminators with thresholds dependent upon E_{cm} and polar angle of the sum, Θ. The

Figure 2.15: A beam's view of the central calorimeter counters (20×64 for $\theta \times \phi$) showing the boundaries of the 40 overlapping super-blocks ($5{\times}8$ for $\Theta{\times}\Phi$); the dashed lines indicate the overlap. The shaded areas are examples of two super-clusters: (Φ, Θ) = (2,1) and (5,3).

thresholds are set at 75% of the expected energy to be deposited by an electron in the super-ring from $\bar{p}p \rightarrow J/\psi + X$ and $J/\psi \rightarrow e^+e^-$. The ring weights in a Level II sum have been determined to normalize the output signals within a super-ring so that electrons that hit anywhere within a super-ring result in the same signal. The discriminator results are used in the hardware trigger.

The other two sets of Level II output signals are sent to FERA ADCs; one set gives the weighted sums for the super-blocks for the trigger interaction and the other set is delayed resulting in a look at the signals in the super-blocks prior to and/or at the beginning of the trigger. The two sets of Level II FERA ADCs' results and the Level I summer pattern units are used to determine pile-up as described in section 6.4.